Supporting Information

for

Accelerating Solar Desalination in Brine through Ions Activated Hierarchically Porous Polyion Complex Hydrogels

Fengbo Zhu,[a,b,#] Liqian Wang,[b,#] Baris Demir,[c,#] Meng An[d], Zi Liang Wu,*[,a] Jun Yin,[e] Rui Xiao*[,b], Qiang Zheng[a], Jin Qian,*[,b]

[a] MOE Key Laboratory of Macromolecular Synthesis and Functionalization, Department of Polymer Science and Engineering, Zhejiang University, Hangzhou, 310027, China

[b] Key Laboratory of Soft Machines and Smart Devices of Zhejiang Province, Department of Engineering Mechanics, Zhejiang University, Hangzhou 310027, China

[c] Centre for Theoretical and Computational Molecular Science, The Australian Institute for Bioengineering and Nanotechnology, The University of Queensland, Queensland, 4072, Australia

[d] College of Mechanical and Electrical Engineering, Shaanxi University of Science and Technology, Xi'an, 710021, China

[e] State Key Laboratory of Fluid Power and Mechatronic Systems, Key Laboratory of 3D Printing Process and Equipment of Zhejiang Province, School of Mechanical Engineering, Zhejiang University, Hangzhou 310028, China

[#] These authors contributed equally to this work.

* Corresponding authors: wuziliang@zju.edu.cn (Z.L.W.), rxiao@zju.edu.cn (R.X.), jqian@zju.edu.cn (J.Q.)

Supplementary Figures and Tables

S1.1 Pore size distributions in HPH

Mercury intrusion porosimetry (AutoPore IV 9510) has been performed to quantitatively examine the porosity in HPH. It was found that the total porosity of HPH is 53.9%, exhibiting a wide distribution of pore diameter from 0.2 μm to 100 μm (Figure S1) and demonstrating the existence of both macro and meso pores in HPH.

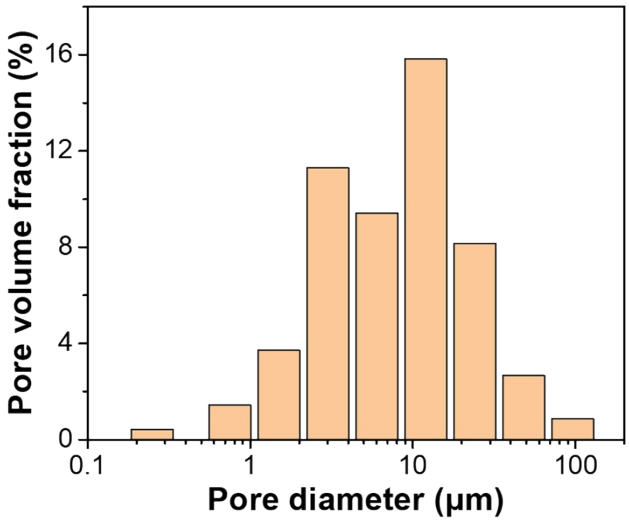

Figure S1. Distribution of pore diameter in HPH obtained from mercury intrusion porosimetry measurement.

S1.2 Micromorphology of as-prepared PIC hydrogel

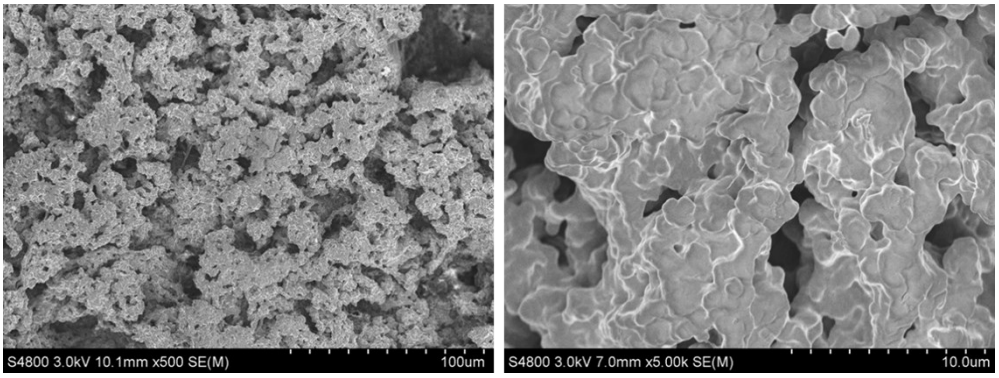

Figure S2. SEM images of as-prepared PIC gel at different magnifications.

S1.3 Fast water absorption driven by capillary force in as-prepared PIC hydrogel

To investigate the contributions of the porous structure to water absorption, a stick-shaped piece of as-prepared PIC hydrogel was frozen dried and dipped into water. It was found that water up-taking occurred instantly and the stick was completely hydrated within 15 seconds, indicating the excellent water absorption ability because of the hierarchically porous structure of HPH (Figure S3).

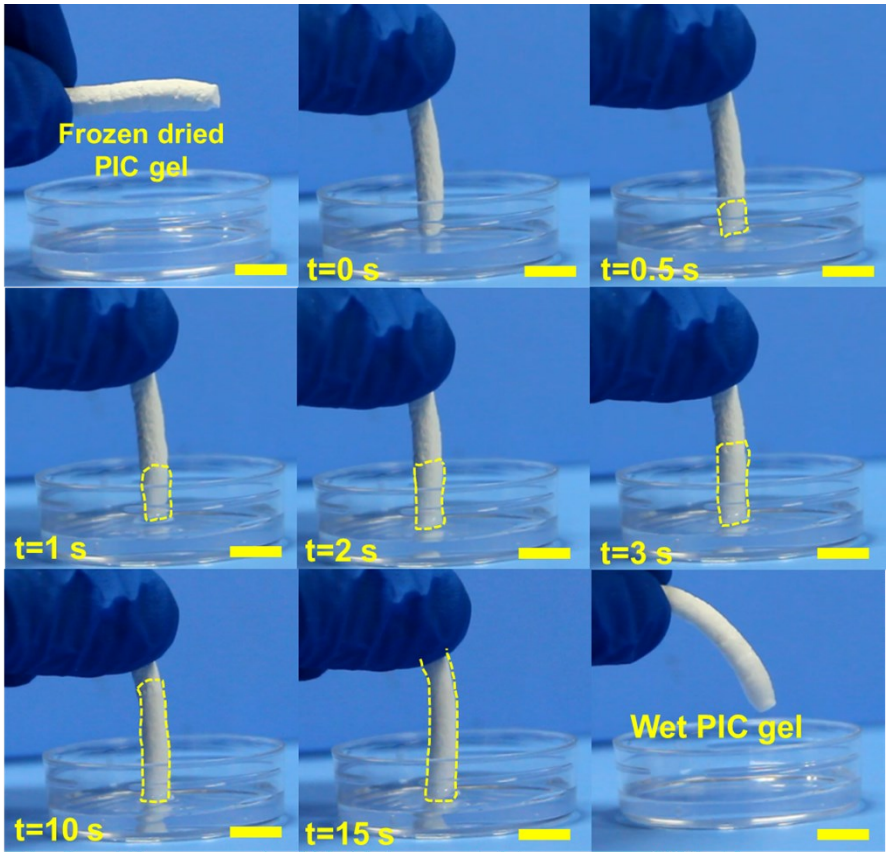

Figure S3. Fast water absorption driven by capillary force in frozen dried as-prepared PIC hydrogel with hierarchical porosity. The dash lines pointed out the hydrated part of PIC stick because of water transport. The scale bars are 1 cm.

S1.4 Solar evaporation performance of HPH without thermal insulator

To demonstrate the effect of involving PS thermal insulator on solar evaporation performance, a control experiment was conducted by removing the thermal insulator from the samples. HPH samples were directly put in pure water and subjected to 1 sun illumination (Figure S4a). Figure S4b presents the corresponding mass change curves, and it is found the evaporation rate without PS foam is 1.35 kg · m^{-2} · h^{-1}, ~20 % lower than the case with PS foam, indicating that thermal management is crucial in enhancing solar vapor generation performance.

It was also found that the concentrations of PAni should be optimized for efficient solar vapor generation (Figure S4b). Because of the intrinsically poor hydrophilicity of PAni, a reduced amount of PAni is beneficial to faster vapor generation in HPH.

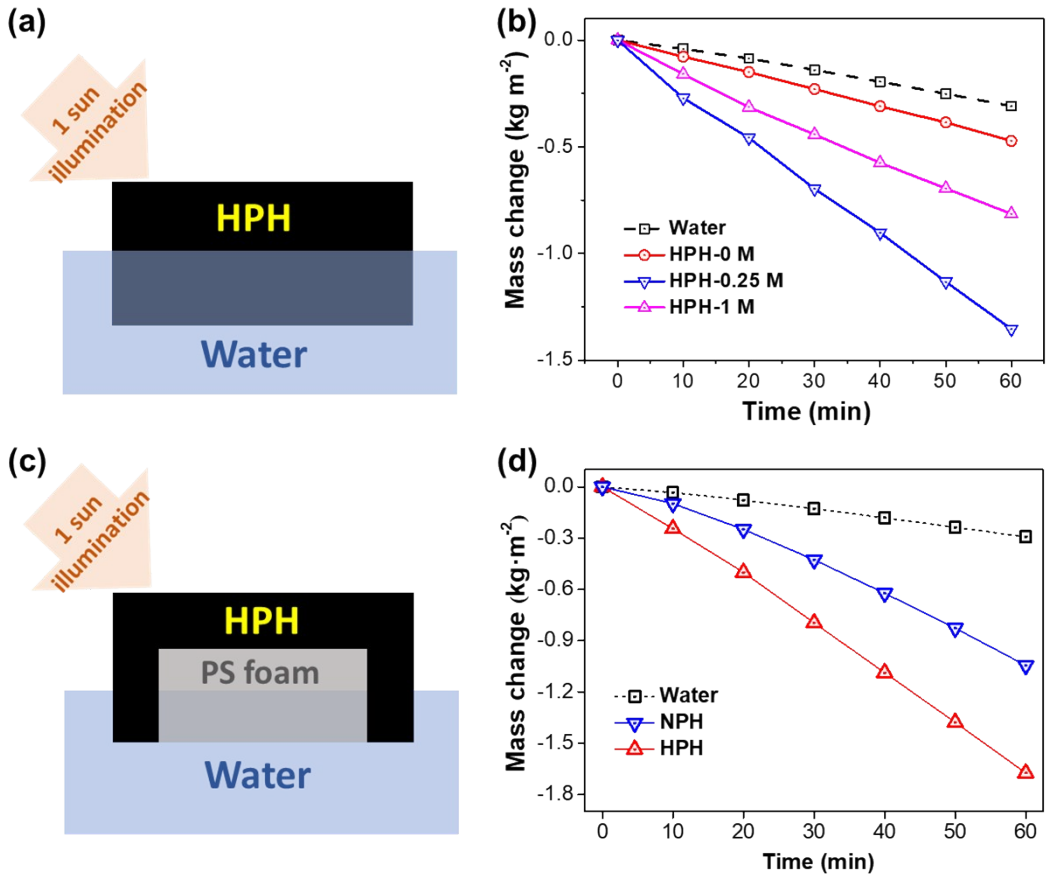

Figure S4. (a,b) Schematic (a) and solar evaporation performance (b) of HPH without thermal

insulator under different PAni concentrations. (c,d) Schematic (c) and solar evaporation performance (d) of HPH and NPH with thermal insulator. All the tests were carried under 1 sun illuminations (1 kW · m^{-2}) in pure water.

S1.5 Solar evaporation performance of NPH in brines of different concentrations

Through a compression moulding process, the obtained PIC/PAni hydrogel showed non-porous surfaces with excellent hydrophilicity, as exhibited in Figure S5a. Even that the surface morphology is non-porous, NPH still exhibited a faster evaporation rate in brines than in pure water (Figure S5b), which was also found in HPH. This consistent trend in both HPH and NPH suggests that the accelerated solar desalination in brines is attributed to the hydration properties of the materials that are sensitive to anions/cations, rather than their porosity.

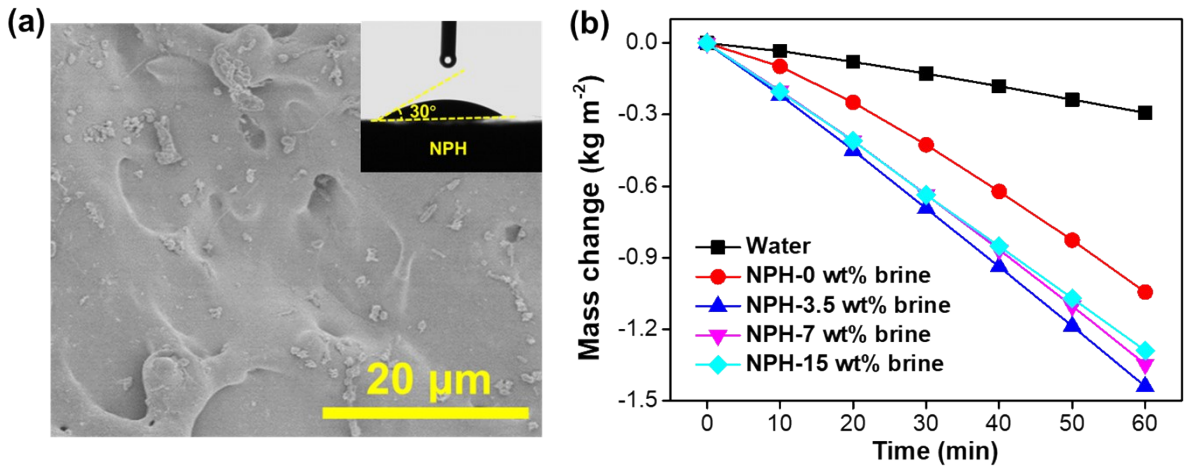

Figure S5. (a) SEM image of surface morphology of NPH. The inset shows the hydrophilicity of NPH through a water contact angle test. (b) Solar desalination performance of NPH in brines of different concentrations under 1 sun illumination.

S1.6 Equivalent vaporization enthalpy of water in HPH with different brine concentrations

To obtain the real vaporization enthalpy, a control experiment was conducted following a standard procedure from previous studies.[1,2] Explicitly, HPH samples with a certain surface area and bulk water with the same exposure area were set in a container, together with the supersaturated potassium carbonate solution under a temperature of ca. 20 ºC and ambient air pressure. For the identical power input U_{in}, the equivalent vaporization enthalpy of water in HPH (ΔH_e) can be calculated through

$$U_{in} = \Delta H_{vap} m_0 = \Delta H_e m_g \quad \text{(S1)}$$

where ΔH_{vap} and m_0 are the evaporation enthalpy and mass change of bulk water, and m_g is the mass change of HPH.

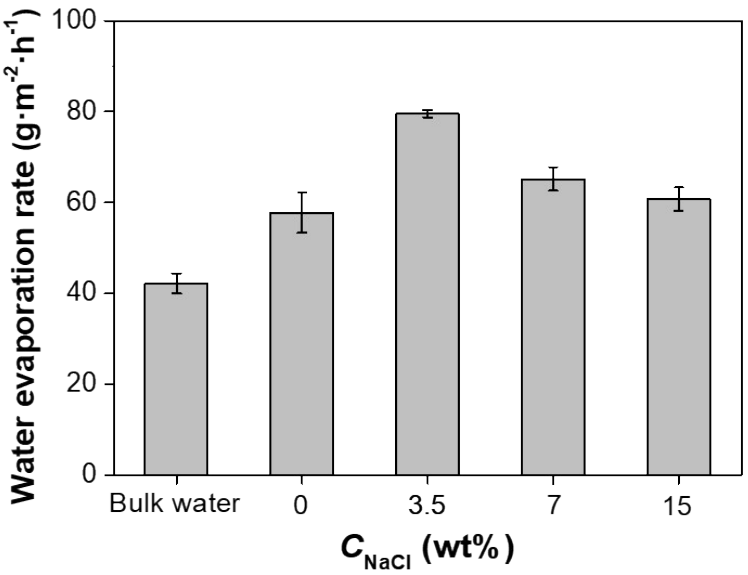

Figure S6. Water evaporation rate in dark condition of bulk water and HPH samples for different brine concentrations.

S1.7 Cyclic solar evaporation performance of HPH-based SVG in different brines.

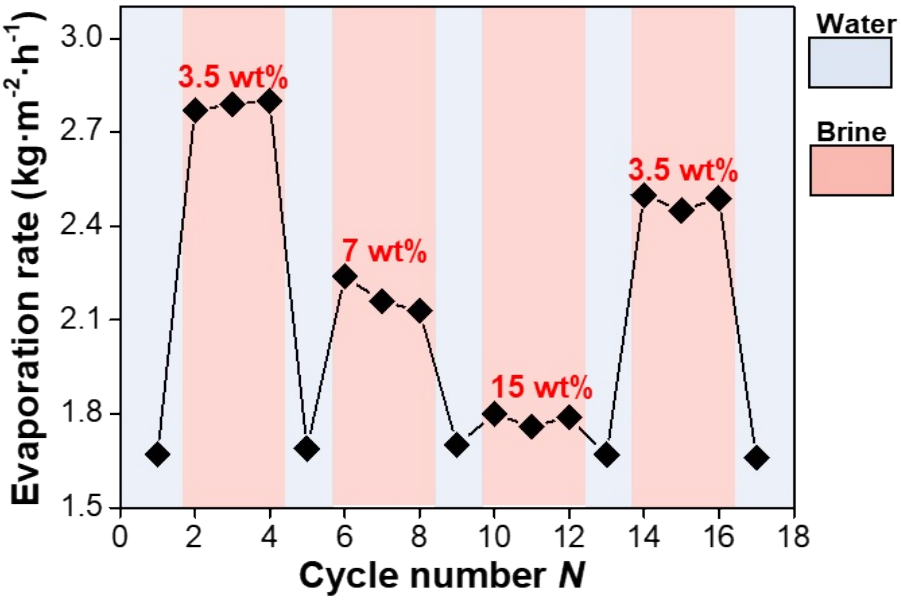

Figure S7. Cyclic solar evaporation rate of HPH-based SVG in different brines under 1 sun.

S1.8 Influence of brine concentrations on the micromorphology of HPH

To confirm whether or not the salt ions will influence the network structure of HPH, we performed the microstructure characterizations. Before the characterizations, HPH was first immersed into brines of different concentrations for 2 d to reach equilibrium and then frozen dried for SEM testing.

As presented in Figure S8, brine concentrations can significantly influence the microscopic morphology of HPH. In pure water, the compactly stacked PIC precipitates form smooth surfaces at 1 μm scale. However, in brine circumstances, the salt ions break the ionic crosslinking of HPH because of electrostatic screening effect. With increasing brine concentrations, the stronger ionic strength can even split PIC precipitates into smaller particles of several hundreds of nm. These findings confirmed the ions mediated tunable networks of HPH in brine circumstances.

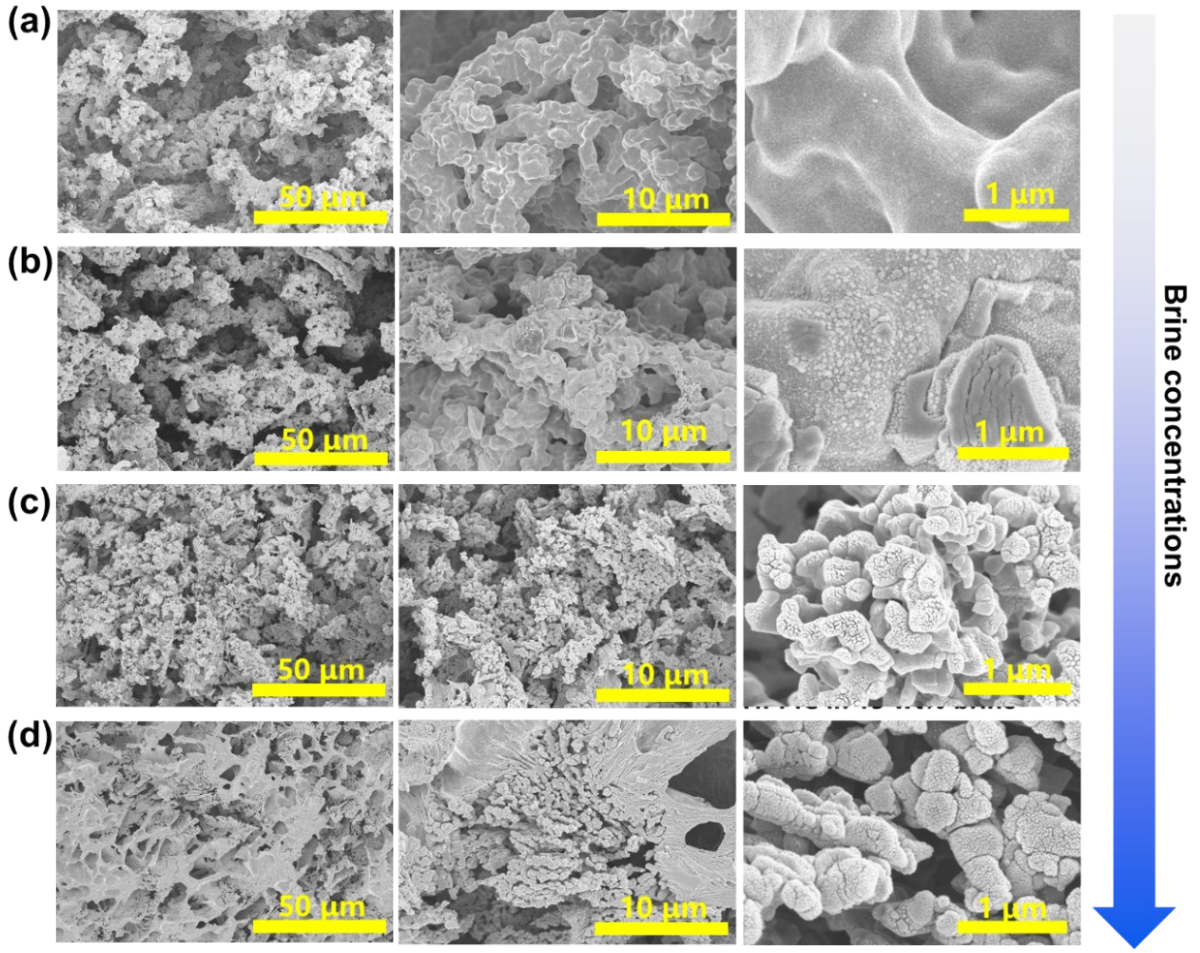

Figure S8. SEM images of HPH at different magnifications with varying brine concentrations. (a) HPH in pure water. (b) HPH in 3.5 wt% brines. (c) HPH in 7 wt% brines. (d) HPH in 15 wt% brines.

S1.9 Variations in water state within HPH in brines of different concentrations

The hydrogen bond networks of water molecules can directly influence gel's physical properties including heat vaporization, thermal conductivity, heat capacity, etc. The degree of disrupted hydrogen bond can be quantitatively measured by analyzing their Raman spectra in the region of O—H stretching.[1,3-5]

Figures S9a-e summarize the Raman spectra of pure water and HPH in brines of different concentrations with fitted Gaussian functions. Each subcomponent is thought to arise from different hydrogen bonding of water. It should be noticed that the exact peak locations of the subcomponents differ from previous studies due to different experimental conditions. However, it has been agreed that the four subpeaks observed from 3150 to 3650 cm^{-1} are related to water.[1,3-5] Take bulk water as an example, the peaks observed at 3225, 3410, 3530, 3630 cm^{-1} can be categorized into two types: water molecules with four hydrogen bonds, i.e., two-proton and two-electron pairs with adjacent water molecules (the peaks at 3225 and 3410 cm^{-1}), which are regarded as free water (FW); weakly or non-hydrogen bonded water molecules (corresponding to the peaks at 3530 and 3630 cm^{-1}), which are considered as intermediate water (IW). Via this approach, we can calculate the molar ratio of IW to FW in bulk water was 0.21, which is consistent with previous research.[1] As a comparison, the molar ratio of IW to FW obtained from HPH in pure water, HPH in 3.5 wt% saline, HPH in 7 wt% saline, and HPH in 15 wt% saline were calculated to be 0.33, 0.49, 0.40, and 0.30. These results indicated that the state of water was greatly altered with varying brine concentrations in HPH, and the increased content of IW leads to a faster vaporization speed of water molecules, as observed in our experiments. The differences in the Raman spectra of HPH reflect the comprehensive influence

of salt and hierarchical porosity on water state. The effects of dissolved NaCl on water have been widely studied, and it has been found that the Raman spectra of NaCl solutions exhibited similar shapes to bulk water but varied from the intensity at different wavenumber.[3,4] The Raman spectra in the region of O-H stretching of HPH is influenced by the polymer networks and surrounding NaCl. At low NaCl concentrations (≤3.5 wt%), the water structure is mainly dominated by HPH-water interactions. However, with increased salt concentrations (≥ 7 wt%), the charged polymers in HPH is mainly doped with ions due to stronger ionic strength. Therefore, the water structure is mainly dominated by the ions-water interactions and the Raman spectra exhibited similar shape to that of pure water.[3,4]

To further verify the ions activated polymer chains of PIC hydrogel, we also investigated their Raman spectra of pure PIC gel (without PAni networks) in the region of O—H stretching and obtained the corresponding ratios of IW to FW from different brines. As shown in Figure S10, salt concentrations clearly affect the Raman spectra of PIC gel; the amount of IW change is slightly different from that of HPH. With increasing salt concentrations, the maximum ratio of IW to FW appears at 7 wt% saline, and then slightly decreases at at 15 wt% saline. This trend is consistent with the MD results of its average hydrogen bond of pure PIC in different brines (Figure 3f of the main text).

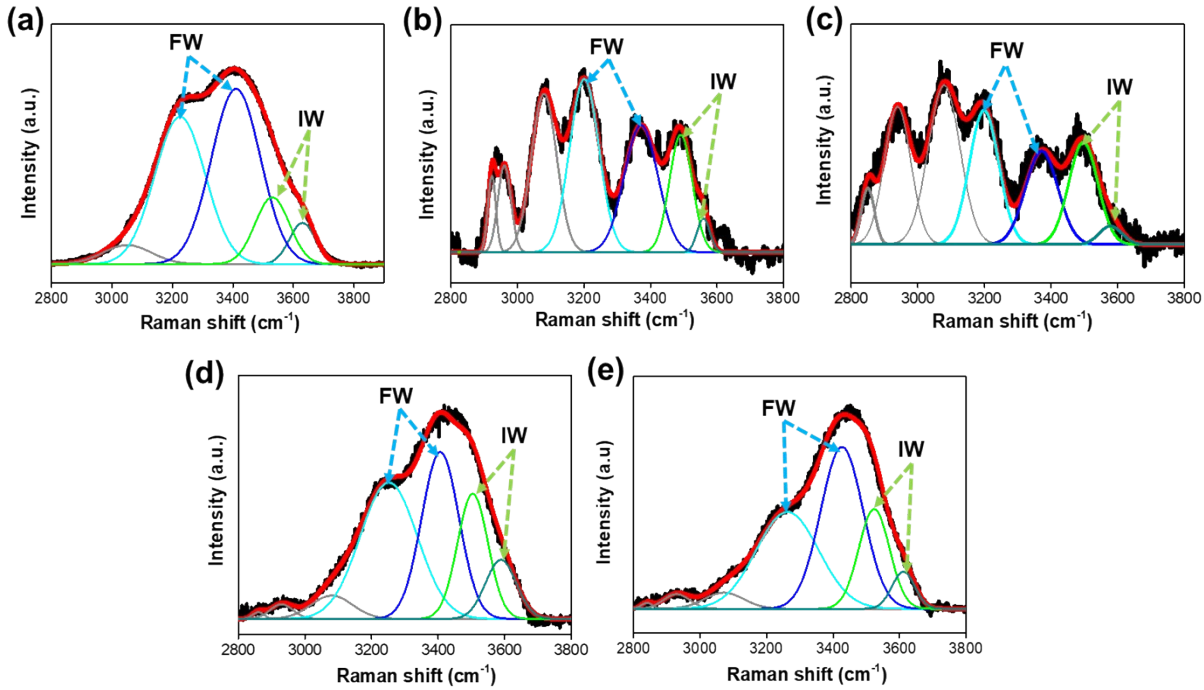

Figure S9. Raman spectra with fitted curves in the energy region of O—H stretching modes for (a) bulk water, (b) HPH in pure water, (c) HPH in 3.5 wt% saline, (d) HPH in 7 wt% saline, and (e) HPH in 15 wt% saline. FW and IW represent free water and intermediate water, respectively.

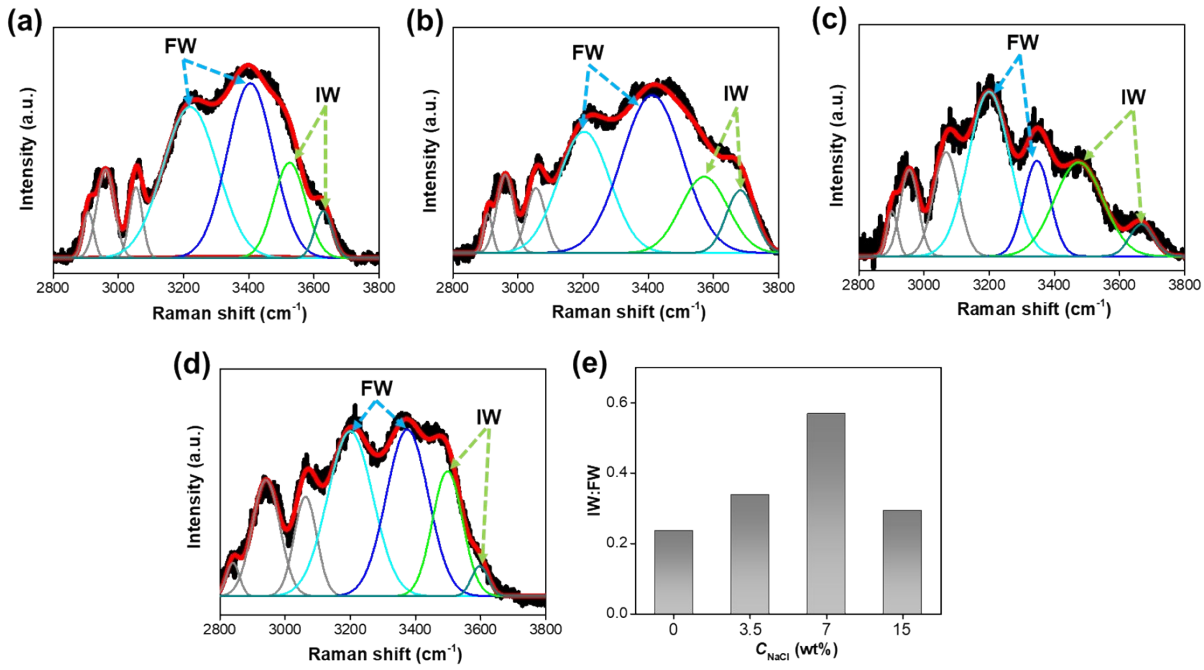

Figure S10. Raman spectra with fitted curves in the energy region of O—H stretching modes for (a) PIC hydrogel in pure water, (b) PIC hydrogel in 3.5 wt% saline, (c) PIC hydrogel in 7 wt% saline, and (d) PIC hydrogel in 15 wt% saline. (e) Corresponding ratios of IW to FW for PIC hydrogel in different brines.

S1.10 Salt-resistant ability of HPH

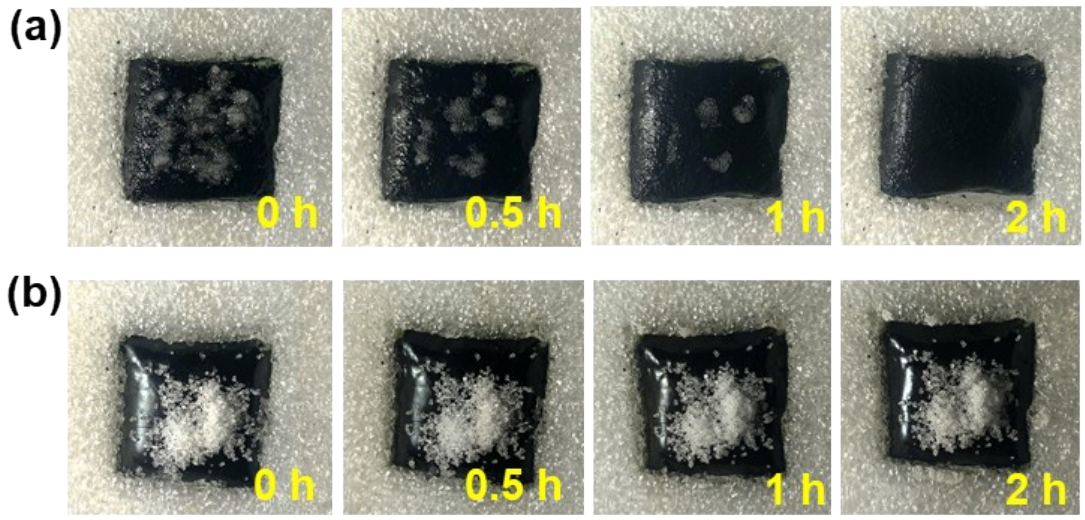

Figure S11. Time-elapsing snapshots that show the salt-resistance of HPH (a) and NPH (b) with the initial presence of salt crystallinity under one sun.

S1.11 Comparison of solar evaporation performance in pure water of various SVGs

Table S1 Comparison of evaporation rate and energy efficiency of various solar vapor generators (test conditions: 1 sun illumination, pure water, room temperature).

Reference	Materials	Evaporation rate $kg \cdot m^{-2} \cdot h^{-1}$	Energy efficiency %
6	3D honeycomb graphene foam	1.30	87.04
7	Graphene oxide/sodium alginate/carbon nanotubes aerogel	1.39	83
8	Vertically aligned graphene sheets	1.62	86.5
9	PEGDA-PAni hydrogel	1.40	91.5
10	Cotton fiber nonwoven fabrics	1.59	93.3
11	Cellulose nanofibrils aerogel	1.11	76.3
12	Au/cotton composite fibers	1.40	86.3
13	Carbon nanosheet frameworks	1.50	93
14	Polyacrylic acid hydrogel coated carbon foam	1.60	79
15	Carbonized mushroom	1.28	78.0
16	Activated carbon fiber felt	1.22	79.4
17	Nitrogen-doxped hydrophilic graphene nanopetals	1.27	88.6
This work	**HPH (PIC-PAni)**	**1.67**	**83.2**

S2 Modelling Section

S2.1 General simulation settings

All-atom molecular dynamics (MD) simulations were used to predict the structure and mechanical properties of the polyelectrolytes. The OPLS force-field was used to describe the inter-atomic interactions.[18] Periodic boundary conditions in all three dimensions were implemented. The Nosé-Hoover thermostat[19,20] and barostat[19,21] were implemented in all simulations to control the temperature and pressure, respectively. The cut-off distance for long-range energy calculations was set to be 12 Å. The contribution of long-range interactions was calculated via the particle-particle-particle-mesh (PPPM) solver.[22] Newton's equations of motion were time-integrated with a time-step of 1 fs using the open-source molecular simulation tool, LAMMPS (lammps.sandia.gov).[23] Visual Molecular Dynamics (VMD) was used to visualize the trajectories generated during simulations.[24]

The initial structures of PNaSS and PMPTC were generated using the freely available AVOGADRO software package.[25] These structures were then geometrically optimized via the use of Generalized Amber Force field (GAFF).[26] The structures were considered to be optimized when the energy difference between two successive iterations dropped below a threshold value (10^{-8} kJ mol^{-1}). We then used these structures as inputs to the calculations of partial atomic charges. We used LigParGen web-based service that provides the OPLS force-field parameters and partial atomic charges for the polyelectrolytes.[27-29] The model used to describe water was the TIP4P-Ew model.

S2.2 Preparation of hydrogel samples

We generated hydrogel samples by placing polyelectrolytes, salt ions, and water molecules together in a cubic simulation box with a dimension of 150 Å using PACKMOL.[30] We adjusted the numbers of polyelectrolytes, salt ions, and water molecules so that the size of each system (in terms of the total number of atoms) was similar (**Table S2**). Each sample was equilibrated via the use of NPT-MD simulations at 294 K and 1 atm over a period of 1 ns.

Table S2. Details of hydrogel models in MD simulations

Salt concentrations (wt%)	10.6	7.2	3.5
Number of each polyelectrolyte monomer	700	450	210
Number of each salt ion	700	450	210
Number of water molecules	5500	10000	14500
Total number of atoms	55000	54750	55050

S2.3 Polymerization procedure

After the equilibration step, we polymerized each sample using the chain-growth polymerization procedure reported in the literature.[31] Each polyelectrolyte was generated separately in the simulation box where all polyelectrolyte monomers, salt ions and water molecules were present. No polymerization was allowed between different polyelectrolyte monomer types. 5% in mol of each polyelectrolyte monomer type was considered as initiators, through which the polymer chains grew. The polymerization procedure was terminated when all the monomers reacted.

S2.4 Structural analysis

Upon the completion of polymerization, the hydrogel samples were equilibrated via the use of NPT-MD simulations at 294 K and 1 atm over a period of 1 ns. Following this, a further 1 ns simulation was performed in the NVT-MD. We tracked a trajectory of 1000 frames that were generated every 1 ps. The whole trajectory was then used for calculating the radial distribution functions (RDFs) and hydrogen bonding analysis.[32]

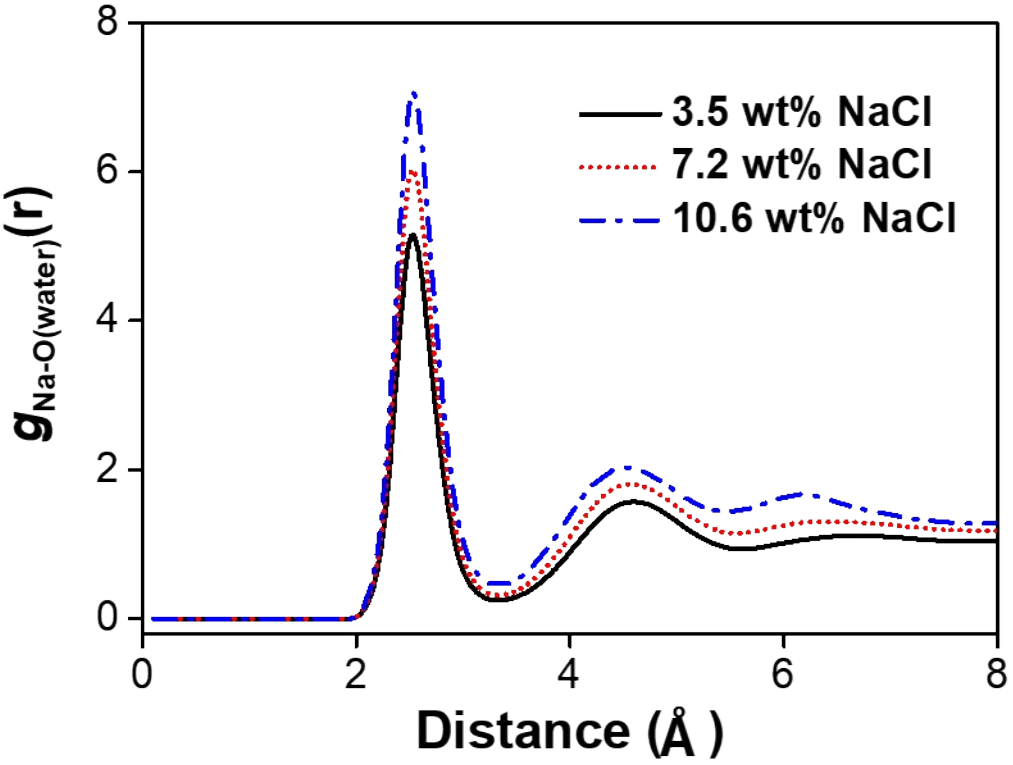

Figure S12. Radial distribution functions (RDFs) between sodium ions and O(water) with varying salt concentrations in PIC.

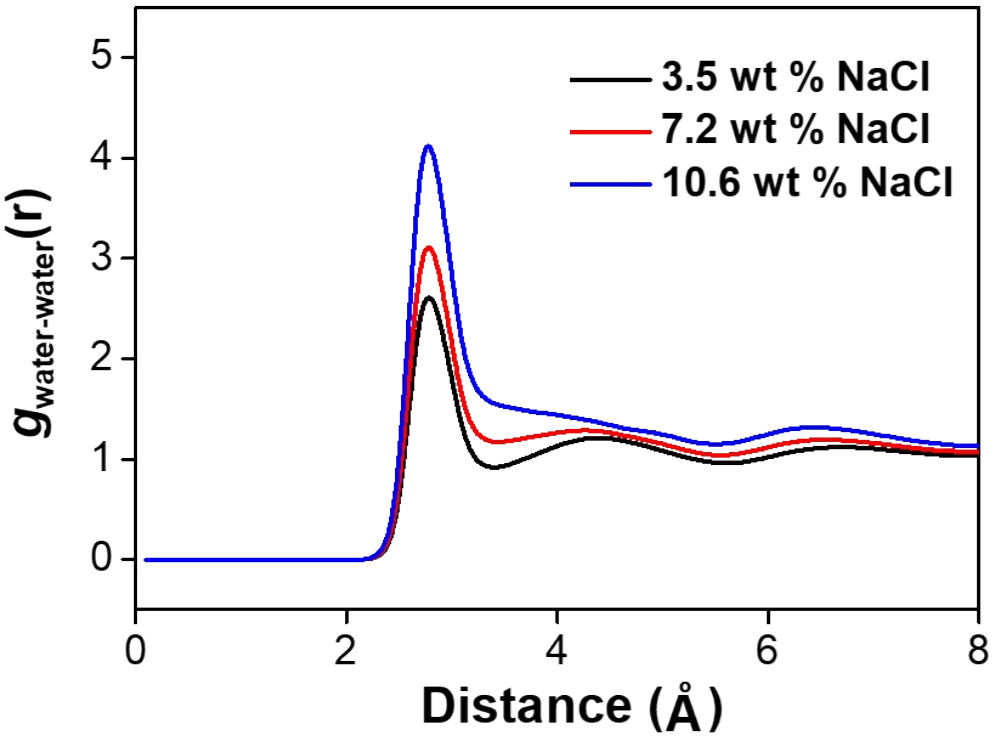

Figure S13. Radial distribution functions (RDFs) between water-water molecules with varying salt concentrations in PIC.

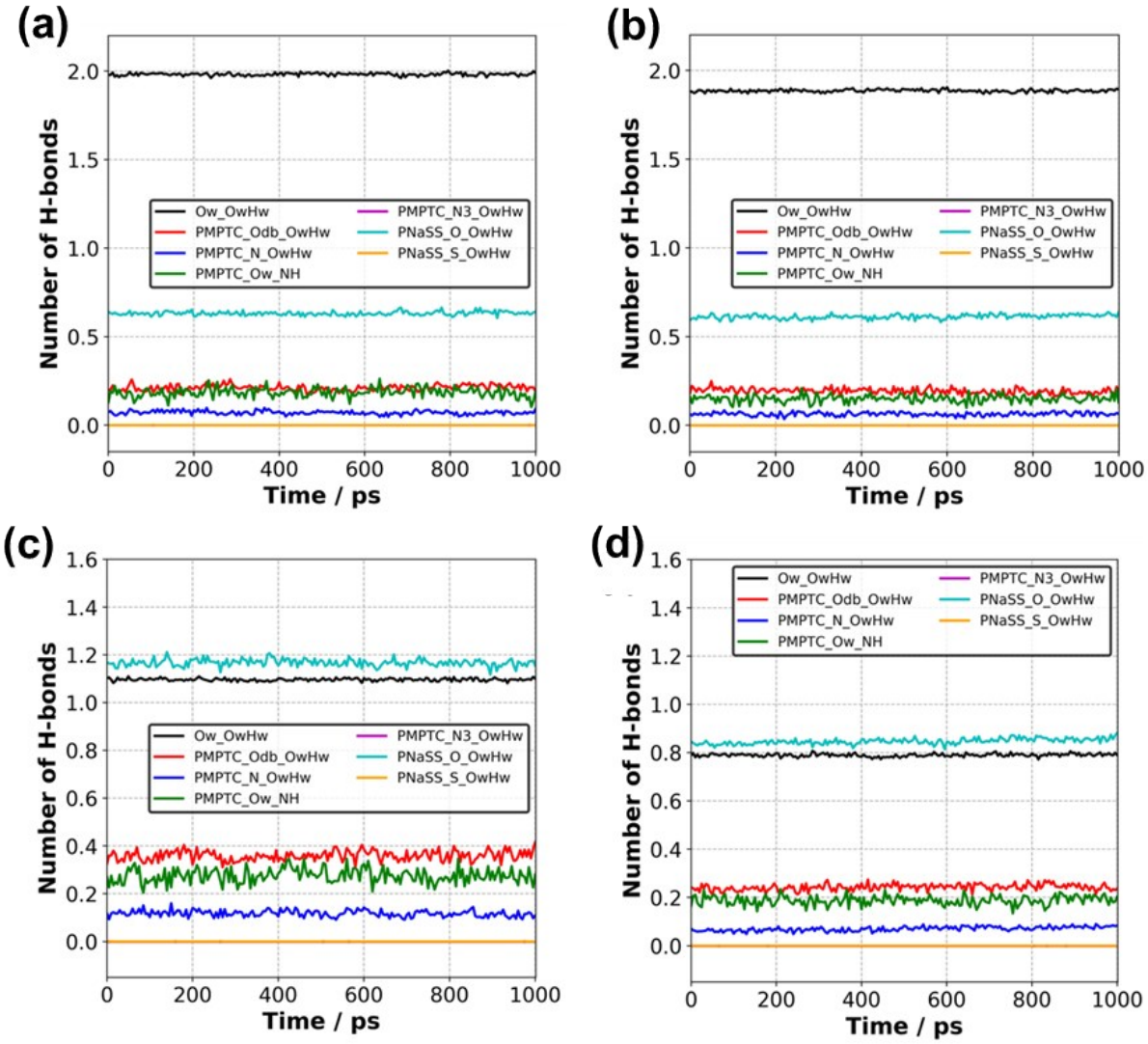

Figure S14. Average number of hydrogen bonds between different pairs in PIC with varying salt concentrations (at 294 K): (a) 0 wt% NaCl, (b) 3.5 wt% NaCl, (c) 7.2 wt% NaCl, and (d) 10.6 wt% NaCl. Ow: water oxygen, Hw: water hydrogen, Odb: carbonyl oxygen, N3: nitrogen atom in $N(CH_3)_3$ group.

S3 Supplementary References

1 F. Zhao, X. Zhou, Y. Shi, X. Qian, M. Alexander, X. Zhao, S. Mendez, R. Yang, L. Qu and G. Yu, *Nat. Nanotechnol.*, 2018, **13**, 489-495.

2 G. Hu, Y. Cao, M. Huang, Q. Wu, K. Zhang, X. Lai, J. Tu, C. Tian, J. Liu, W. Huang and L. Ding, *Energy Technol-Ger*, 2020, **8**, 1900721.

3 X. Wu, W. Lu, W. Ou, M. C. Caumon and J. Dubessy, *J. Raman Spectrosc.*, 2017, **48**, 314-322.

4 Q. Sun, *Vib. Spectrosc.*, 2012, **62**, 110-114.

5 H. Kitano, K. Nagaoka, S. Tada and M. Gemmei-Ide, *J. Colloid Interf. Sci.*, 2007, **313**, 461-468.

6 Y. Yang, R. Zhao, T. Zhang, K. Zhao, P. Xiao, Y. Ma, P. M. Ajayan, G. Shi and Y. Chen, *ACS Nano*, 2018, **12**, 829-835.

7 X. Hu, W. Xu, L. Zhou, Y. Tan, Y. Wang, S. Zhu and J. Zhu, *Adv. Mater.*, 2017, **29**, 1604031.

8 P. Zhang, J. Li, L. Lv, Y. Zhao and L. Qu, *ACS Nano*, 2017, **11**, 5087-5093.

9 X. Yin, Y. Zhang, Q. Guo, X. Cai, J. Xiao, Z. Ding and J. Yang, *ACS Appl. Mater. Interfaces*, 2018, **10**, 10998-11007.

10 Q. Fang, T. Li, H. Lin, R. Jiang and F. Liu, *ACS Appl. Energy Mater.*, 2019, **2**, 4354-4361.

11 F. Jiang, H. Liu, Y. Li, Y. Kuang, X. Xu, C. Chen, H. Huang, C. Jia, X. Zhao and E. Hitz, *ACS Appl. Mater. Interfaces*, 2018, **10**, 1104-1112.

12 H. D. Kiriarachchi, F. S. Awad, A. A. Hassan, J. A. Bobb, A. Lin and M. El-Shall, *Nanoscale*, 2018, **10**, 18531-18539.

13 L. Sun, J. Liu, Y. Zhao, J. Xu and Y. Li, *Carbon*, 2019, **145**, 352-358.

14 J. Zeng, Q. Wang, Y. Shi, P. Liu and R. Chen, *Adv. Energy Mater.*, 2019, **9**, 1900552.

15 N. Xu, X. Hu, W. Xu, X. Li, L. Zhou, S. Zhu and J. Zhu, *Adv. Mater.*, 2017, **29**, 1606762.

16 H. Li, Y. He, Y. Hu and X. Wang, *ACS Appl. Mater. Interfaces*, 2018, **10**, 9362-9368.

17 S. Wu, G. Xiong, H. Yang, B. Gong, Y. Tian, C. Xu, Y. Wang, T. Fisher, J. Yan, K. Cen, T. Luo, X. Tu, B. Zheng and K. Ostrikov, *Adv. Energy Mater.*, 2019, **9**, 1901286.

18 W. L. Jorgensen, D. S. Maxwell and J. Tirado-Rives, *J. Am. Chem. Soc.*, 1996, **118**, 11225-11236.

19 S. Nosé, *J. Chem. Phys.*, 1984, **81**, 511-519.

20 W. G. Hoover, *Phys. Rev. A*, 1985, **31**, 1695-1697.

21 W. G. Hoover, *Phys. Rev. A*, 1986, **34**, 2499-2500.

22 R. Hockney and J. Eastwood, *Computer Simulation using Particles*, 1989, Adam Hilger.

23 S. Plimpton, *J. Comput. Phys.*, 1995, **117**, 1-19.

24 W. Humphrey, A. Dalke and K. Schulten, *J. Mol. Graph.*, 1996, **14**, 33-40.

25 M. Hanwell, D. Curtis, D. Lonie, T. Vandermeersch, E. Zurek and G. Hutchison, *J. Cheminform.*, 2012, **4**, 17.

26 J. Wang, R. M. Wolf, J. W. Caldwell, P. A. Kollman and D. A. Case, *J. Comput. Chem.*, 2004, **25**, 1157-1174.

27 W. L. Jorgensen and J. Tirado-Rives, *Proc. Natl. Acad. Sci. U.S.A.*, 2005, **102**, 6665-6670.

28 L. S. Dodda, J. Z. Vilseck, J. Tirado-Rives and W. L. Jorgensen, *J. Phys. Chem. B*, 2017, **121**, 3864-3870.

29 L. S. Dodda, I. Cabeza de Vaca, J. Tirado-Rives and W. L. Jorgensen, *Nucleic Acid. Res.*, 2017, **45**, 331-336.

30 L. Martínez, R. Andrade, E. G. Birgin and J. M. Martínez, *J. Comput. Chem.*, 2009, **30**, 2157-2164.

31 B. Demir and T.R. Walsh, *ACS Appl. Polym. Mater.*, 2019, **1**, 3027-3038.

32 B. Demir, *Polymer*, 2020, **191**, 122253.